ISSN: 1692-7257 - Volume 1 – Issue 47 - 2026

ORIGINAL

RCTA
Revista Colombiana de Tecnologías de Avanzada
UNIPAMPLONA

Identification of asbestos-cement in NIR images via spectral similarity and artificial neural networks

Identificación de asbesto-cemento en imágenes NIR mediante métodos de similitud espectral y redes neuronales artificiales

Gabriel Elías Chanchí Golondrino[1]
Manuel Alejandro Ospina Alarcón[1]
Manuel Saba[2]

[1] **Universidad de Cartagena, Facultad de Ingeniería, Prog. de Ingeniería de Sistema, Cartagena, Bolívar, Colombia.**
[2] **Universidad de Cartagena, Facultad de Ingeniería, Prog. de Ingeniería Civil, Cartagena, Bolívar, Colombia.**

Received: 26 July 2025. Revised: 26 September 2025. Accepted: 20 December 2025. Published: 01 January 2026.
Corresponding Author: Gabriel Elías Chanchí Golondrino

How to cite: G. E. Chanchí Golondrino, M. A. Ospina Alarcón, and M. Saba, "Identificación de asbesto-cemento en imágenes NIR mediante métodos de similitud espectral y redes neuronales artificiales", *Revista Colombiana de Tecnologías de Avanzada (RCTA)*, vol. 1, no. 47, ene. 2026, art. no. 4108, doi: 10.24054/rcta.v1i47.4108

This work is licensed under a Creative Commons Attribution-NonCommercial 4.0 International License.

Abstract:

This study employs airborne multispectral imagery obtained from the repository of the Environmental Public Agency of Cartagena (EPA), which provides a spatial resolution of 0.17 m/pixel. The dataset consists of four spectral bands (R, G, B, and NIR), from which 300 spectral signatures of asbestos–cement roofing and 300 signatures of other materials were extracted. The labeling was conducted through visual interpretation supported by field visits. Two configurations of the data cube were evaluated: one containing the four multispectral bands and another with five bands, generated by incorporating the first principal component obtained through PCA. Three spectral similarity measures (Cosine-Based Similarity (CBS), Spectral Distance Similarity (SDS), and Euclidean Distance Similarity (EDS)) were compared along with an artificial neural network (ANN) model. The performance was assessed using a 70–30 split based on precision, recall, F1-score, and execution time. The results indicate that EDS and CBS achieved the highest detection accuracy, with EDS being computationally more efficient (CBS was 2.22 times slower). These findings demonstrate that EDS and CBS are promising methods for the efficient detection of asbestos–cement roofing from multispectral imagery and can be extrapolated to the identification of other materials under similar spatial-resolution and data-quality conditions.

Keywords: Asbestos-cement, multispectral images, spectral similarity,artificial neural networks.

Resumen:

Este estudio emplea imágenes multiespectrales aéreas obtenidas a partir del repositorio del Establecimiento Público Ambiental de Cartagena (EPA), las cuales cuentan con una resolución espacial de 0.17 m/píxel. El conjunto de datos está compuesto por cuatro bandas espectrales (R, G, B y NIR), a partir de las cuales se extrajeron 300 firmas espectrales de cubiertas de asbesto-cemento y 300 firmas de otros materiales. El etiquetado se realizó mediante interpretación visual apoyada en visitas de campo. Se evaluaron dos configuraciones del cubo de datos: una con las cuatro bandas multiespectrales y otra con cinco bandas, generada mediante la incorporación del primer componente principal obtenido mediante PCA. Se compararon tres medidas de similitud espectral (Cosine-Based Similarity (CBS), Spectral Distance Similarity (SDS) y Euclidean Distance Similarity (EDS)) junto con un modelo de red neuronal artificial (ANN). El desempeño se evaluó mediante división 70–30 utilizando métricas de precisión, recall, F1 y tiempo de ejecución. Los resultados indican que EDS y CBS alcanzaron la mayor exactitud en la detección, siendo EDS computacionalmente más eficiente (CBS fue 2,22 veces más lento). Estos hallazgos demuestran que EDS y CBS son métodos prometedores para la detección eficiente de cubiertas de asbesto-cemento a partir de imágenes multiespectrales, y pueden ser extrapolados a la identificación de otros materiales bajo condiciones similares de resolución espacial y calidad de datos.

Palabras clave: Asbesto-cemento, imágenes multiespectrales, similitud espectral, redes neuronales artificiales.

INTRODUCTION

Remote sensing is a technique that consists of identifying, measuring and analyzing the characteristics of objects or areas of the Earth's surface without entering into direct contact, using the detection and recording of electromagnetic energy reflected or emitted by them[1],[2]. To this end, remote sensing uses sensors installed on satellites, aircraft or drones, which operate in different parts of the electromagnetic spectrum (visible, infrared, microwave, etc.)[3],[4]. Compared with traditional methods, remote sensing offers several advantages for environmental monitoring: it allows large areas of terrain to be monitored in a short time without requiring physical contact with the study area, which facilitates continuous observation and the tracking of changes over time[5]-[8].

Among the most widespread remote sensing techniques, spectral imagery stands out. It can be defined as imagery that captures information from a scene in multiple bands of the electromagnetic spectrum, allowing the composition and characteristics of the observed objects to be analyzed; for this reason, such imagery is considered a "data cube", since it organizes information in three dimensions: two spatial dimensions (x,y) and one spectral dimension (wavelength) . Spectral imagery includes both multispectral imagery, which contains dozens of bands, and hyperspectral imagery, which includes hundreds of bands; in both cases, this imagery provides detailed information on the reflectance or emission of materials at different wavelengths .

Several studies have been conducted in the field of spectral imagery. Thus, in[13], models supported by convolutional neural networks were used to detect asbestos-cement on RGB and NIR aerial images, achieving detection precision of 89%, validating the usefulness of these methods for large-scale inventories. Likewise, in[14], quantitative mapping of asbestos-cement roofing was carried out in an extensive mountainous region of the Italian Alps covering 3263km using multispectral imagery obtained from the MVIDIS sensor, achieving detection precision of 80% and concluding that the spatial resolution of the data constitutes the main source of detection errors. On the other hand, in[15]-[17], hyperspectral imagery in the SWIR range (1100-2500 nm) was used to detect asbestos in cement matrices, using models such as SIMCA and PLS-DA, demonstrating high sensitivity and specificity (0,89–1,00) in detection. Likewise, in[18]the use of Mask R-CNN with multispectral satellite imagery (MSSI) and high-resolution aerial imagery (HRAI) was evaluated for the detection of fibrocement roofs on Australian residential buildings, obtaining detection precision of 94% and a confidence threshold of 99.8%. On the other hand, in[19], hyperspectral imagery and the ENVI software were used for the mapping and diagnosis of the condition of asbestos-cement roofs in the urban area of the city of Cartagena de Indias, identifying that up to 47% of the surface area of some neighborhoods was covered by this material, with an average of 20% at the neighborhood level and more than 9 km² throughout the city. In this same vein, in[20], the effectiveness of a computational method based on the identification of prominent peaks in the spectral signature of asbestos-cement was evaluated, assessing said method effectively on hyperspectral imagery of 380 bands from Cartagena de Indias.

Regarding the challenges of hyperspectral imagery, a first point is that, because these images contain hundreds of spectral bands, they generate data cubes with a large volume of information that hinders their analysis; for environments with limited memory, their processing therefore usually requires efficient partitioning and storage techniques[21]-[23]. Likewise, processing these images with complex methods such as deep learning demands great computational power and cost, so these methods are not suitable for real-time monitoring applications[24]-[26]. In this context, lighter models or dimensionality reduction techniques are therefore needed to balance detection precision and speed[27],[28]. For multispectral imagery, since the number of bands is reduced compared with hyperspectral imagery, the precise identification of materials with similar spectral signatures is difficult[29]-[31]. Likewise, with multispectral imagery, identifying materials in complex mixtures or in overlapping layers is difficult, because the spectral signature may be a combination of several materials[29].

Given the challenges of processing and analyzing the large amount of data contained in hyperspectral images, and the challenge for multispectral imagery of enabling material detection with few bands, this article proposes as a first contribution the evaluation of methods based on spectral similarity (correlation (CBS), spectral differential similarity (SDS), Euclidean distance (EDS) and artificial neural networks (ANN)) for detecting asbestos-cement in 4-band NIR-type multispectral imagery of the city of Cartagena de Indias. It also proposes evaluating these four methods on a new version of the images in which a new band or layer corresponding to the PCA (Principal Component Analysis) principal component of the image was added, in order to identify whether the detection capabilities of each evaluated method improve. Thus, given the lower economic cost of acquiring NIR images and the lower computational cost of processing them, this work presents a competitive alternative for identifying roofs containing asbestos, which is of great interest to government authorities in Colombia and in other developing countries seeking to mitigate the harmful effects of this material on human health. Likewise, this work is intended to be replicated and extrapolated at the academic and business level for the evaluation of these methods in the detection of other materials, taking advantage of the NIR image enrichment technique by means of a fifth band derived from the PCA principal component.

Recent studies have explored the use of lightweight convolutional neural networks (CNN), support vector machines (SVM) and classical methods based on spectral angles, such as SAM and SID, for detecting materials on roofs and for multispectral

classification in general. Lightweight CNNs often achieve high performance by incorporating spatial information; however, they depend on larger annotated datasets, data augmentation techniques and training schemes oriented toward GPU use[32],[33].

SVMs, for their part, have been widely used in multispectral and hyperspectral classification because they are robust to small sample sizes, although they generally require careful hyperparameter tuning and do not offer explicit spectral interpretability . SAM and SID continue to be used as references because of their stability and well-understood spectral behavior; however, their performance tends to decrease when the number of available spectral bands is limited .

In this same sense, independent validation is common practice in remote sensing applications, especially when the reliability of ground reference data is uncertain. These strategies usually rely on field survey campaigns, auxiliary cadastral layers or high-resolution reference images in order to cross-verify roof materials or land cover types . In this context, the dataset was carefully refined through visual inspection and controlled sampling to ensure its internal consistency and adequate interpretability.

Within this framework, the present work contributes through the systematic comparison of three spectral similarity measures (CBS, SDS and EDS) against a simple artificial neural network, using only four spectral bands and one PCA-derived component. This comparison provides a realistic baseline for low-band-count airborne multispectral scenarios, in which the use of advanced hyperspectral sensors, extensive field reference data or GPU-intensive architectures is not viable.

In recent studies on roofing material detection, most approaches are based on hyperspectral sensors or computationally intensive models, such as convolutional neural network (CNN)-based architectures and high-dimensional spectral classifiers. These methods usually require large data volumes, specialized acquisition systems or GPU-oriented processing modules. In contrast, the present work focuses on a lightweight, low-band-count multispectral approach, using only four spectral bands (R, G, B and NIR), together with an additional component derived through principal component analysis (PCA).

Thus, the main contribution of this article lies in the comparison of three spectral similarity measures (CBS, SDS and EDS) against an artificial neural network with a simple structure, using a small and fully interpretable dataset obtained from real urban structures. The study highlights the computational efficiency, reproducibility and practical feasibility of implementing these methods within low-cost workflows, in contexts where high-end hyperspectral sensors are not available. This aspect is particularly relevant for developing countries such as Colombia, where asbestos has recently been banned and large-scale assessment of asbestos-cement roofing is urgently required.

The remainder of the article is organized as follows: Section 2 presents the methodological phases that guided the development of this research. Section 3 presents the results derived from this research, which first includes the fitting and evaluation of the detection capability of the 4 methods with sample spectral signatures of asbestos-cement and of other materials derived from 4- and 5-band images. It also includes the deployment of the 4 methods on an NIR image of areas surrounding the Cerro de la Popa in Cartagena, visually verifying the areas detected by each method. It further includes the evaluation of the computational efficiency of each method in the processing and analysis of a 30x30 pixel region of the image, where each pixel has 5 spectral bands. Finally, Section 4 includes the conclusions and future work derived from this research.

METHODOLOGY

For the development of this research, the CRISP-DM methodology was adapted into four phases: F1. Business and data understanding, F2. Data preparation, F3. Modeling and evaluation, F4. Model deployment (see Figure 1).

The CRISP-DM methodology was chosen because its clear structure in standardized phases facilitates the organization and understanding of the life cycle of data science projects, allowing clear management from problem understanding to the implementation, deployment and maintenance of models .

The CRISP-DM methodology is also highly adaptable: it can be integrated with agile approaches or customized for specific application contexts, as is the case of computer vision .

In phase 1 of the methodology, from a reference aerial multispectral image of 3000 × 3000 pixels and four spectral bands of reflectance (red, green, blue and near-infrared), a total of 600 pixels or sample spectral signatures were selected by visual inspection and field validation, of which 300 corresponded to asbestos-cement roofing and 300 to other materials. The aerial multispectral images used in this study were obtained from publicly accessible datasets published by the Public Environmental Establishment (EPA) of Cartagena and, although their coverage spans the entire urban area of the city, the analysis focused specifically on the region corresponding to Cerro de La Popa. According to the technical information associated with the published data, the images had previously undergone spatial resampling and radiometric correction processes, so the analysis was performed directly using the standardized spatial resolution and the corrected radiometric values provided in the dataset. The procedure described was likewise applied to an equivalent image of five spectral bands, where the fifth band incorporated was obtained from the first principal component derived from the application of principal component analysis (PCA) to the original four-band image.

The preprocessing of the images consisted of converting the source files into a structured multispectral data cube, removing evident outliers and independently normalizing each spectral band in order to reduce the variability associated with lighting conditions. As previously mentioned, a version of the dataset with five bands was also generated by calculating and incorporating the normalized first principal component obtained from principal component analysis (PCA). These procedures ensured consistent input representations for both the spectral similarity measures and the artificial neural network model. Given the absence of absolute radiometric calibration records, the study focuses on the analysis of relative spectral behavior, rather than absolute reflectance values.

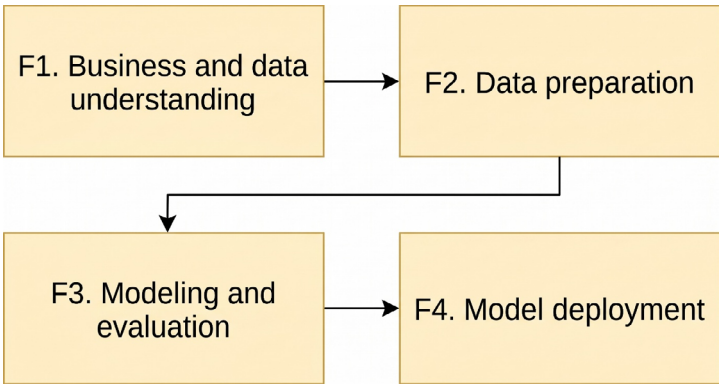

Fig. 1. *Methodology considered.*
Source: own elaboration.

The 600 spectral signatures used in this work were selected through a structured procedure validated in the field. Asbestos-cement (AC) roofing was identified using a methodological framework adapted from previous studies and adjusted to the specific characteristics of the dataset analyzed. In that previous study, conducted in the urban area of Cartagena, physical roofing samples (1 × 1 cm) were collected from representative buildings and analyzed by polarized light microscopy (PLM) in accordance with ASTM D7521-22 to confirm the presence of asbestos fibers. These verified asbestos-cement roofing locations served as reference sites for spectral characterization and class labeling in the present study. The remaining roofing material classes were delineated through detailed visual interpretation and field verification. Each sampled roof was georeferenced using GPS coordinates and, where available, supported by auxiliary cadastral information, such as property boundaries and building footprints, to ensure the spatial and material consistency of the samples.

The same set of spatial locations was used for both the four-band and the five-band dataset to preserve consistency across experiments. Thus, in phase 1 two independent datasets were created, one corresponding to the four-band image and the other to the five-band image, each consisting of 300 sample pixels and subdivided into two classes: asbestos-cement and other materials. The stability of the spectral responses and the low noise levels present in the images allowed the extraction of consistent and reproducible spectral signatures for subsequent analysis.

These sample pixels or spectral signatures were used to fit and evaluate the 4 methods considered in this article in order to identify the detection capability of each method and, in the case of the spectral similarity methods, to determine the reference thresholds from which the methods detect the material. Note that, to convert the image from tif format to a data cube or three-dimensional array, advantage was taken of the rasterio library in Python, which allows the original data cube to be converted into a multidimensional array of the numpy library type in Python.

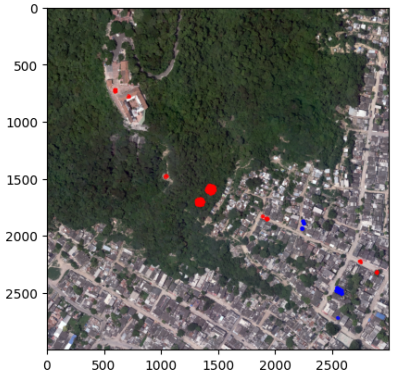

Fig. 2. *Sample pixels of asbestos-cement and other materials.*
Source: own elaboration.

On this basis, Figure 2 shows, over an RGB representation of the multispectral image of areas surrounding the Cerro de la Popa, the location of the selected sample pixels, where asbestos-cement pixels are shown in blue and pixels of other materials are shown in red.

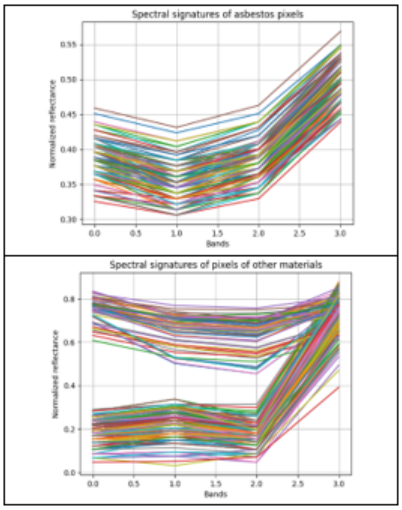

Fig. 3. *Spectral signatures of the 4-band pixels.*
Source: own elaboration.

Figure 4 presents, based on the same 600 sample points, the 300 asbestos-cement spectral signatures and the 300 signatures of other materials, obtained from the 5 spectral bands image.

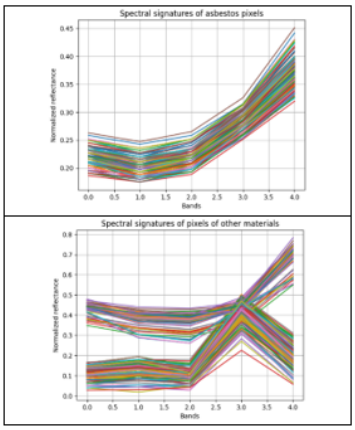

Fig. 4. *Spectral signatures of the pixels of 5 bands.*
Source: own elaboration.

In phase 2 of the methodology, for the 3 methods based on spectral similarity, the average spectral signatures or characteristic spectral signatures associated with the asbestos-cement sample pixels of 4 and 5 bands were calculated. This was done using the advantages provided by the numpy library, which allows the band-by-band calculation of the average reflectance, thus obtaining the two average spectral signatures of 4 and 5 bands, respectively.

These two signatures were subsequently used to calculate the similarity with the two groups of sample pixels and to determine the detection thresholds and the detection capability of the spectral similarity methods. As for the artificial neural network ANN model, 2 datasets derived from the labeling of the sample spectral signatures of 4 and 5 bands, respectively, were assembled.

Consequently, the final dataset consisted of 300 records corresponding to spectral signatures of asbestos-cement roofing, labeled as class 1, and 300 records corresponding to spectral signatures of other materials, labeled as class 0. This dataset was used for the training, hyperparameter tuning and performance evaluation of the artificial neural network (ANN) model.

For the artificial neural network (ANN) model, the dataset was split into a training set and a test set following a 70/30 ratio. Given the limited number of columns available in the dataset, the ANN model was included only as a lightweight baseline, and not as a fully generalizable classifier. No cross-validation scheme was applied, since the aim of the study was not to optimize a high-capacity learning model, but to compare its behavior against the spectral similarity methods under the same

reduced input conditions.

It should also be noted that, although the selection of 300 asbestos-cement samples could be interpreted as a limitation, these points belong to the same material with homogeneous characteristics and, therefore, present highly similar spectral signatures, which makes it unnecessary to collect thousands of samples of this material. However, one of the possible limitations when extrapolating this study lies in the identification, through field visits, of suitable areas where the material is present and where representative samples can be obtained.

Likewise, in phase 3 of the methodology, the first step was the implementation and evaluation of the 3 similarity methods based on correlation, spectral differential similarity and Euclidean distance, using the two groups of sample pixels, both of 4 and of 5 bands, in order to identify the detection capacity of each method and therefore the minimum detection thresholds, verifying that the minimum percentage of similarity with asbestos-cement pixels is higher than the maximum percentage of similarity with other materials. These thresholds are key for the deployment of the spectral similarity methods over the entire image, since they indicate the levels from which these methods classify pixels as asbestos-cement. Specifically, the mathematical equation that represents correlation-based similarity (CBS), implemented in this phase, is presented in(1), where r is the normalized Pearson correlation, which when calculated by the SciPy library of Python is in the range of 0 to 2 and determines the degree of similarity between the patterns or trends of two arrays, in this case the correlated spectral pixels.

$$CBS = (\frac{r+1}{2})x100 \quad (1)$$

Likewise, equation (2) represents spectral differential similarity (SDS), where Xi and Yi correspond to the two compared arrays, in this case the average pixel and a specific pixel of the image. N corresponds to the number of bands of the image, in this case 4 or 5. SDS thus sums the band-by-band reflectance differences of the two arrays, so that the smaller the difference, the more similar the compared arrays or spectral signatures are.

$$SDS = 100 - (\frac{\sum(X_i - Y_i)}{N})x100 \ (2)$$

Equation (3) represents spectral similarity based on Euclidean distance (EDS), where Xi and Yi are the compared arrays, previously normalized, while ED is the normalized Euclidean distance of the arrays Xi and Yi. ED measures the straight-line distance between two spectral arrays in an N-dimensional space, where N is the number of spectral bands.

$$EDS = \left(1 - \frac{ED(Xi, Yi)}{\sqrt{2}}\right) x\ 100 \quad (3)$$

As for the ANN model, in this phase the architecture of the models to be applied to the 6-band dataset and the 7-band dataset was designed and implemented using the tensorflow library of Python, and their performance was evaluated over 100 epochs, taking the accuracy metric as a reference. The architectures were evaluated iteratively until the most consistent results and the best performance on the training and test sets were obtained. Specifically, equation (4) mathematically represents the architecture of the artificial neural network (ANN), where Xi represents the inputs of the neuron, wi corresponds to the weights associated with each input, b is the polarization or bias term, f is the activation function (such as ReLU, tanh, sigmoid) and $\hat{y}$is the estimated output generated by the neuron.

$$\hat{y} = f\left(\sum_{i=1}^{n} \omega_i x_i + b\right) \quad (4)$$

Finally, once the fitting capacity of each method had been identified, phase 4 of the methodology deployed each of the four methods considered on the multispectral images of 4 and 5 reflectance bands, using the thresholds detected in phase 3 for the spectral similarity methods, in order to obtain the percentage of asbestos-cement for each method and visually compare the areas detected in each case. In this phase we also compared the computational efficiency of each method by running them on a 30x30 pixel region of the image with 5 reflectance bands at a different number of repetitions: 25, 50, 75 and 100, in order to obtain the average processing time per repetition and the average total processing time, which was used to evaluate the relative computational efficiency among the methods.

Thus, to ensure that the execution time results were not affected by the variability associated with a single run, each method was executed multiple times on the same 30 × 30 pixel image region with five spectral bands. Four repetition levels were used (25, 50, 75 and 100 runs), and the reported values correspond to the average processing time obtained from these repetitions.

This repetition approach provides a basic measure of temporal stability, even though confidence intervals are not reported, since the main objective of this experiment was to compare the relative efficiency of the methods rather than to perform an exhaustive statistical analysis of performance.

All experiments were carried out in an academic computing environment using Google Colab, executed on a Linux-based operating system with 12.7 GB of available RAM. No GPU acceleration was used. This description of the execution environment is included to contextualize the time comparisons, which reflect relative differences among the methods and not absolute execution times.

Processing times were measured using the time module built into Python, which records the real-time duration required for each run. Only the core computation of each algorithm was included in the measurement; the data loading and preprocessing stages were excluded to avoid bias in the comparison.

RESULTS AND DISCUSSION

At the level of results, first, the average spectral signatures of the asbestos-cement sample pixels of 4 and 5 bands were obtained, which are presented in Figure 5. These signatures were used to evaluate the asbestos-cement detection capacity of the 3 spectral similarity methods in the two groups of sample pixels, both of 4 and of 5 reflectance bands.

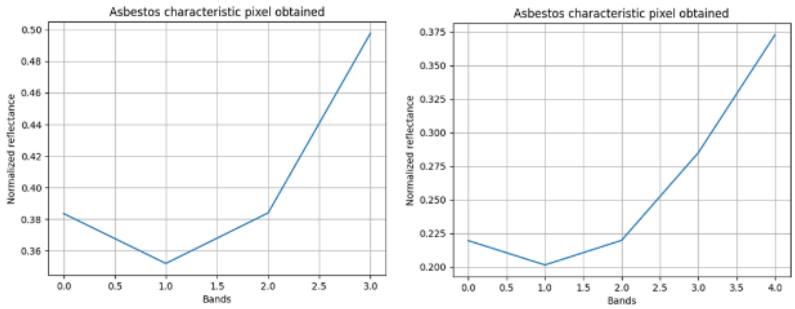

Fig. 5. *Average spectral signature obtained for the sample pixels of 4 and 5 bands.*
Source: own elaboration.

Similarly, for the ANN model, two datasets of 600 instances each were built, associated respectively with the sample pixels of 4 and 5 bands. The first dataset thus has 600 instances in 5 columns: the first four hold the reflectance values (RGB bands and NIR band) and the last holds the label for the pixel type, 1 for asbestos-cement pixels and 0 for pixels of other materials. The second dataset consisted of 6 columns: the first 5 hold the reflectance values of the 4 bands of the first dataset plus an additional band associated with the first principal component of PCA applied to the image. The sixth column holds the label for the pixel type, as in the first dataset. Figure 6 shows the structure of the second dataset, which, as mentioned, includes an additional band on top of the information in the first dataset.

	band1	band2	band3	band4	pixel
0	0.396078	0.352941	0.380392	0.513725	1.0
1	0.407843	0.360784	0.380392	0.509804	1.0
2	0.396078	0.368627	0.400000	0.517647	1.0
3	0.403922	0.352941	0.380392	0.501961	1.0
4	0.403922	0.368627	0.400000	0.513725	1.0
...	...	...	...	...	...
595	0.215686	0.239216	0.207843	0.800000	0.0
596	0.180392	0.227451	0.152941	0.745098	0.0
597	0.168627	0.192157	0.168627	0.713725	0.0
598	0.254902	0.298039	0.196078	0.819608	0.0
599	0.270588	0.313725	0.258824	0.796078	0.0

600 rows × 5 columns

Fig. 6. *Dataset obtained for the 5-band image.*
Source: own elaboration.

Starting from the average spectral signatures obtained from the asbestos-cement sample pixels of 4 and 5 bands, the 3 spectral similarity methods considered were implemented and evaluated: CBS, SDS and EDS. These determined, in 3 different mathematical ways, how similar the characteristic spectral signatures of 4 and 5 bands are to the two groups of sample pixels. As mentioned previously, the three methods were implemented using the advantages for mathematical operations between arrays provided by the scipy and numpy libraries. Figure 7 presents the comparative results obtained by the 3 spectral similarity methods with the 2 groups of pixels of 4 reflectance bands.

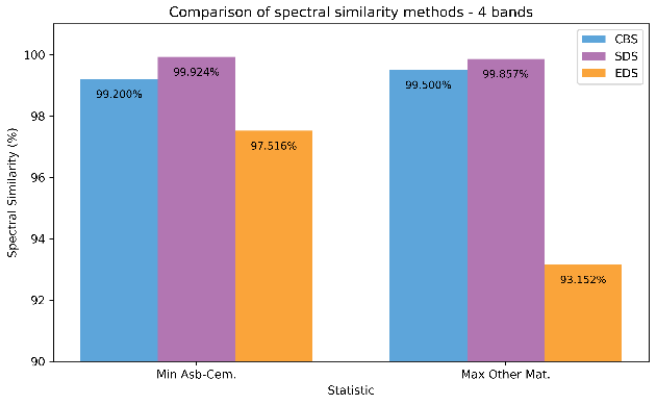

Fig. 7. *Comparison of spectral similarity methods with sample pixels of 4 bands.*
Source: own elaboration.

According to the results in Figure 7, for the sample pixels of 4 bands the only method that shows overlap is CBS: the minimum spectral similarity percentage with the 300 asbestos-cement sample pixels is not greater than the maximum similarity percentage with pixels of other materials. The SDS and EDS methods show no overlap and allow a clearer differentiation of the characteristic spectral signature of asbestos-cement from those of other materials, with a difference between thresholds of 0.067% for SDS and 4.364% for EDS. Although the SDS method has the highest minimum similarity percentage of the group, the EDS method provides the greatest differentiation of the spectral signature with respect to the sample pixels of other materials.

Figure 8 presents the comparative results obtained by the 3 spectral similarity methods with the two groups of pixels of 5 reflectance bands. Unlike the evaluation with the 4-band sample pixels, the 3 methods considered do not overlap: in all 3 cases the minimum similarity with asbestos-cement pixels is greater than the maximum similarity with pixels of other materials. For the CBS method, the difference between the two thresholds went from negative to 2.3%, while for the SDS and EDS methods the difference decreased slightly, from 0.067% to 0.027% and from 4.364% to 3.479%, respectively. Thus, although the additional band slightly reduces the detection capacity of the SDS and EDS methods, the CBS method clearly differentiates the characteristic spectral signature of pixels of other materials, with a percentage difference between thresholds of 2.3%.

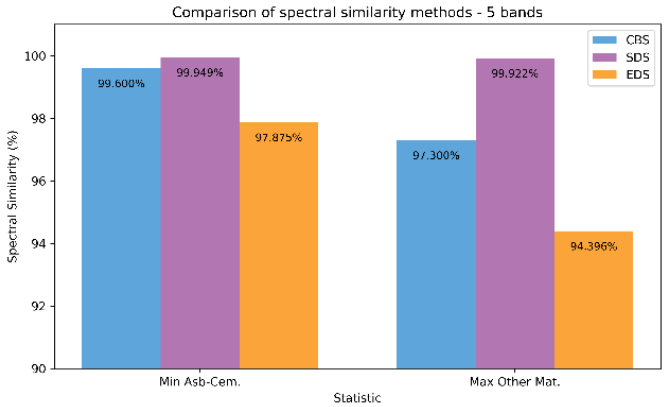

Fig. 8. *Comparison of spectral similarity methods with 5-band sample pixels.*
Source: own elaboration.

Accordingly, although the correlation method improved with the 5 bands in its capacity to differentiate the spectral signature of asbestos-cement from pixels of other materials, the EDS method still shows the greatest difference in the thresholds and therefore provides the best detection capacity with the sample pixels.

Continuing with the ANN model, the architecture was designed and tuned with the training and test sets derived from the 4 reflectance band dataset. The best fit occurs when the sequential model is structured with an input layer of 4 neurons, an output layer of 1 neuron due to the binary nature of the problem, and 3 hidden layers of 12, 8 and 4 neurons. ReLU activation functions were used in the hidden layers and a Sigmoid function in the output layer. For regularization, a Dropout layer with a rate of 20% was applied after each layer, including the input and hidden layers, to prevent overfitting. The model was compiled using the Adam optimizer with a learning rate of 0.001, and 'binary_crossentropy' was used as the loss function, suitable for binary classification, together with the 'accuracy' metric as the main metric to evaluate performance. Figure 9 presents the structure of the ANN model and the implementation code in TensorFlow.

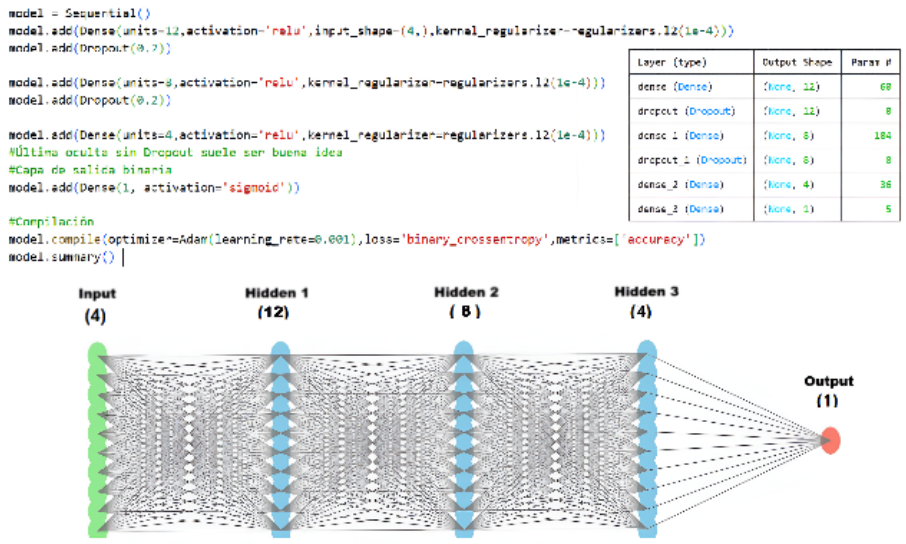

Fig. 8. *Structure of the ANN for the 4 spectral band dataset.*
Source: own elaboration.

Likewise, for the 5-band dataset, the ANN model obtained a similar structure: an input layer with 5 neurons, an output layer with one neuron given the binary nature of the problem, and three hidden layers with 12, 8, and 4 neurons, with the other parameters and functions the same as the ANN model for the 4-band dataset.

The structure of the models was evaluated iteratively over 100 epochs with the training and test sets of the 4- and 5-band datasets. For the ANN model associated with the 4-band dataset and presented in Figure 8, this yielded both the performance based on the accuracy metric and the losses across the different epochs in training and in evaluation, as presented in Figure 9.

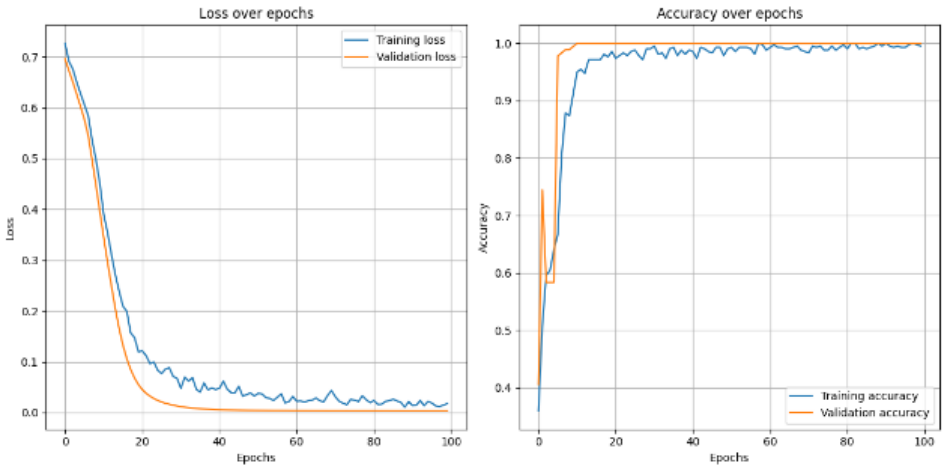

Fig. 9. *Performance of the ANN model of the 4-band dataset.*
Source: own elaboration.

Figure 9 shows that the training loss decreases sharply during the first epochs and then progressively stabilizes at values close to 0.05 from approximately epoch 40 onward, with slight oscillations typical of the optimization process. The validation loss decreases consistently in a similar way and remains at comparable values, slightly lower than those of training, which

suggests adequate convergence of the model with no evidence of overfitting. As for the accuracy metric, the training precision increases rapidly and reaches values above 0.95 around the first 15–20 epochs, subsequently stabilizing near 1.0. The validation precision follows a very similar trend, reaching values close to unity in the early stages of training, which indicates a high level of performance and a notable generalization capacity of the ANN model on the 4-band dataset evaluated.

Likewise, regarding the evaluation of the 5-band ANN model, Figure 10 presents the results for the losses and the performance of the model over 100 epochs in the training and test sets.

According to Figure 10, the training loss of the ANN model trained with the 5 spectral bands dataset decreases rapidly and sharply during the first epochs, progressively stabilizing at values close to 0.03–0.05 from approximately epoch 35–40 onward, with slight oscillations associated with the iterative optimization process. Consistently, the validation loss follows a similar trend, reaching values slightly lower than those of training and remaining stable throughout training, which suggests adequate convergence of the model with no signs of overfitting.

Regarding the accuracy metric, the training precision increases rapidly and exceeds values of 0.95 in the first 15–20 epochs, subsequently stabilizing at values close to unity. The validation precision shows a practically identical behavior, reaching values close to 1.0 in the early stages of training, which evidences a high level of performance and a remarkable generalization capacity of the ANN model upon incorporating additional spectral information in the 5-band dataset. Thus, compared with the model trained with the 4-band dataset, the inclusion of the additional band results in slightly faster convergence and greater stability in both loss and precision, suggesting a marginal benefit in the model's learning process.

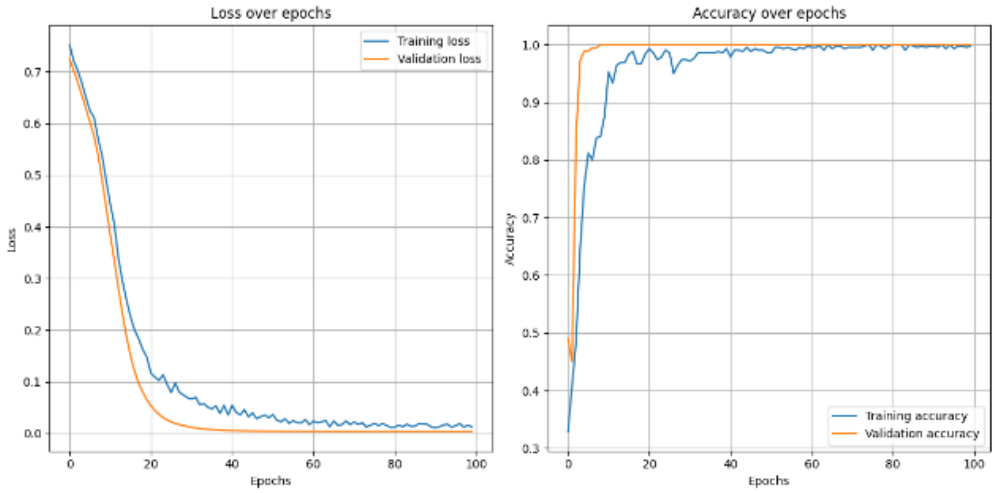

Fig. 10. *Performance of the ANN model of the 5-band dataset.*
Source: own elaboration.

In this sense, Figure 11 presents the average performance achieved by the ANN model over the last 20 of the 100 epochs considered, in terms of the metrics derived from the confusion matrix, such as precision, recall and F1-score for both the 4-band dataset and the 5-band dataset.

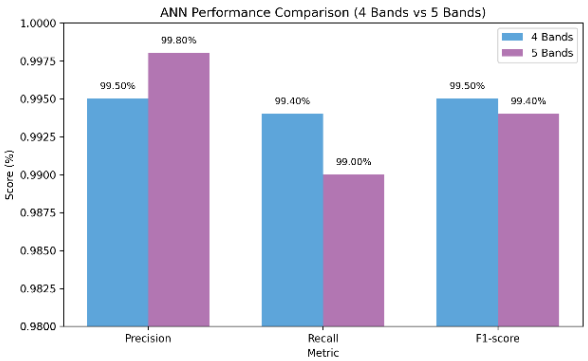

Fig. 11. *Performance metrics of the ANN model for the 4- and 5-band datasets.*
Source: own elaboration.

From the results presented in Figure 11, the three metrics considered (precision, recall and F1-score) reach values above 99%

in both datasets, which indicates a globally high and consistent performance of the evaluated models. In particular, the ANN model trained with the 4-band dataset shows a slightly higher performance in the recall and F1-score metrics, which suggests a greater capacity to correctly identify the class of interest and a better balance between precision and recall.

The ANN model evaluated on the 5-band dataset, in turn, shows a higher performance in the precision metric, indicating a reduction in the proportion of false positives, possibly associated with the incorporation of additional spectral information. However, the differences observed between both configurations are marginal, which suggests that the ANN model remains robust to variations in the number of spectral bands considered.

In order to deploy the 3 spectral similarity methods and the sequential ANN model over the complete 4-band multispectral image, each pixel of the 4-band image was iterated and classified in an RGB representation of the multispectral image, after applying the similarity and classification operations with the four methods. Figure 12 presents in blue the asbestos pixels detected by each of the four methods over an RGB image representation.

From the results presented in Figure 12, it is visually apparent that the EDS and CBS methods detect asbestos-cement pixels most precisely in the 4-band image, with a percentage of pixels of 6.89% and 5.639%, respectively. Likewise, although the SDS method detects close to double the pixels (13.083%) than the EDS and CBS methods, it makes more detection errors, identifying asbestos pixels in the upper part of the Cerro de la Popa, where the presence of asbestos-cement is not evident.

This method also confuses more road and vegetation pixels than the CBS and EDS methods. Finally, although the ANN model obtained a good performance in the fitting and detects the greatest number of asbestos pixels, with 19.772%, it is also the method that makes the greatest number of errors, confusing vegetation and road pixels with asbestos-cement pixels, which makes its percentage of asbestos pixels the highest of the 4 methods.

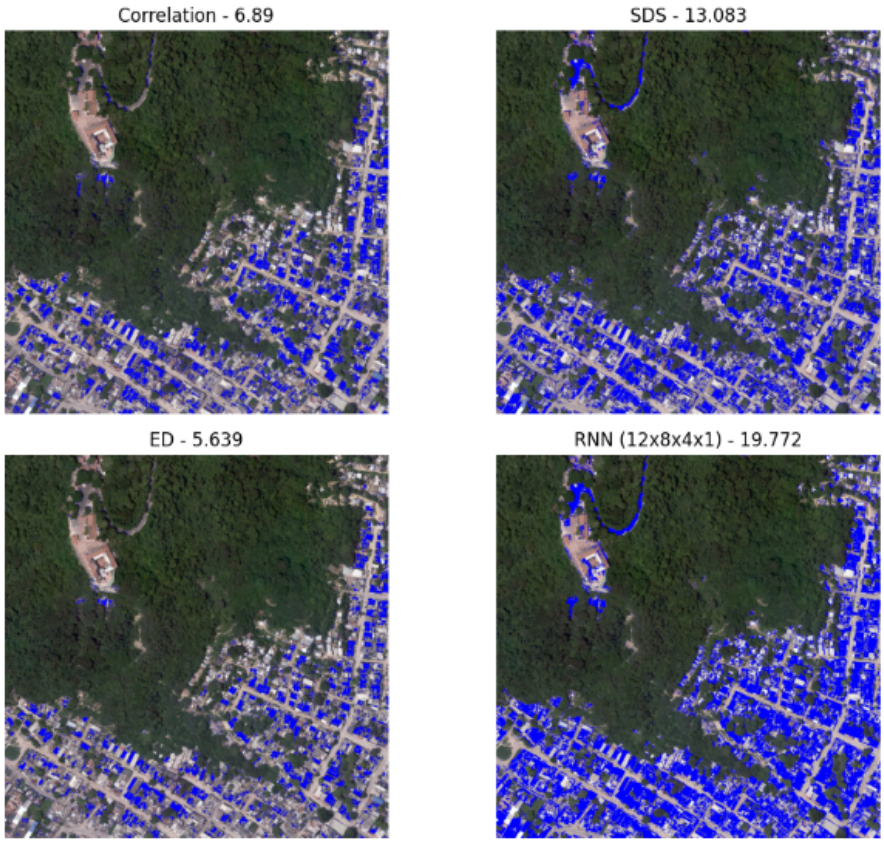

Fig. 12. *Deployment of the 4 methods over the 4-band multispectral image.*
Source: own elaboration.

When the 4 methods considered were implemented and deployed on the multispectral image with 5 bands (4 reflectance bands and one additional band obtained from the PCA analysis), the asbestos-cement pixels were classified, such that Figure 13 presents in blue the asbestos-cement pixels detected on an RGB representation of the image using the 4 methods considered.

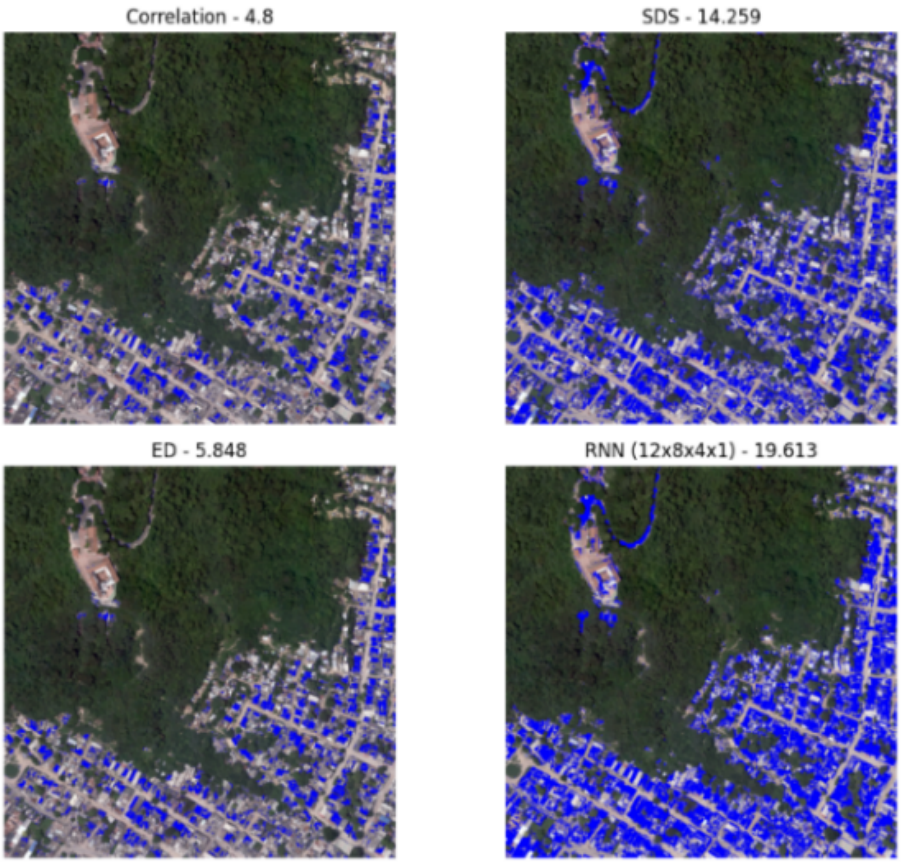

Fig. 13. *Deployment of the 4 methods on the 5-band multispectral image.*
Source: own elaboration.

According to the results presented in Figure 13, the EDS and CBS methods continue to present the best detection results, slightly increasing the detection percentage for the EDS method and slightly decreasing it for the CBS method with respect to the detection performed on the 4-band image. Likewise, the SDS method obtained a slightly higher percentage than with the 4-band image, such that errors continue to appear in the upper part of the Cerro de la Popa, as well as confusion in the vegetation and road pixels. For the ANN model, the detection percentage decreased slightly with respect to the 4-band image, reducing detection errors and therefore the confusion of vegetation and road pixels with asbestos-cement pixels. Thus, by including an additional band in the 4-band image, the CBS and ANN methods refine the detection, while the EDS method presents similar detection results and the SDS method slightly decreases its detection capacity, increasing the number of errors.

However, in order to comparatively evaluate the computational efficiency of the 4 methods considered, they were deployed in multiple repetitions (25,50,75 and 100) over a 30x30 region of the image with 5 spectral bands, using the Python timeit library and in order to identify the processing time per repetition, the average processing time and the relative efficiency of the methods. Thus, Figure 14 presents a line diagram showing the processing time obtained by each of the methods in the different repetitions.

From the results presented in Figure 14, it can be seen that the ANN model is the one that on average takes the longest time across the different repetitions, so that in processing the 30x30 pixels image with 5 reflectance bands it takes a minimum time of 92.8 milliseconds and a maximum time of 130.2 milliseconds. On the other hand, among the spectral similarity methods, the one that is on average most efficient is SDS, followed closely by the EDS method and, with a larger difference, by the CBS method, with no overlap in the curves of the 3 methods; that is, the SDS method has shorter times than the EDS method across the different repetitions, and in turn the EDS method has shorter times across the different repetitions than the CBS method. Since the methods with the greatest detection efficacy were EDS and CBS, it is important to compare the relative efficiency between them, taking into account first of all that the EDS method takes, in processing the image region, average times ranging between 9.5 and 15.9 milliseconds, whereas the CBS method takes average processing times ranging between 20 and 36 milliseconds. Now, when comparing the overall average across the different repetitions of the EDS and CBS methods, it is found that on average the CBS method is 2.22 times slower than the EDS method, which indicates that in terms of time reduction the EDS method reduces by 54.76% the time taken by the CBS method.

Now, regarding the discussion of the results obtained, it should be mentioned that this work evaluated the feasibility of using spectral similarity methods and methods based on sequential neural networks for the identification of asbestos-cement roofing in multispectral imagery of 4 bands (RGB + NIR) and in NIR images enriched with a fifth band corresponding to the first PCA component of the image. As a result, it was found that the EDS and CBS methods were the ones that presented, overall, the best efficacy and efficiency in detection.

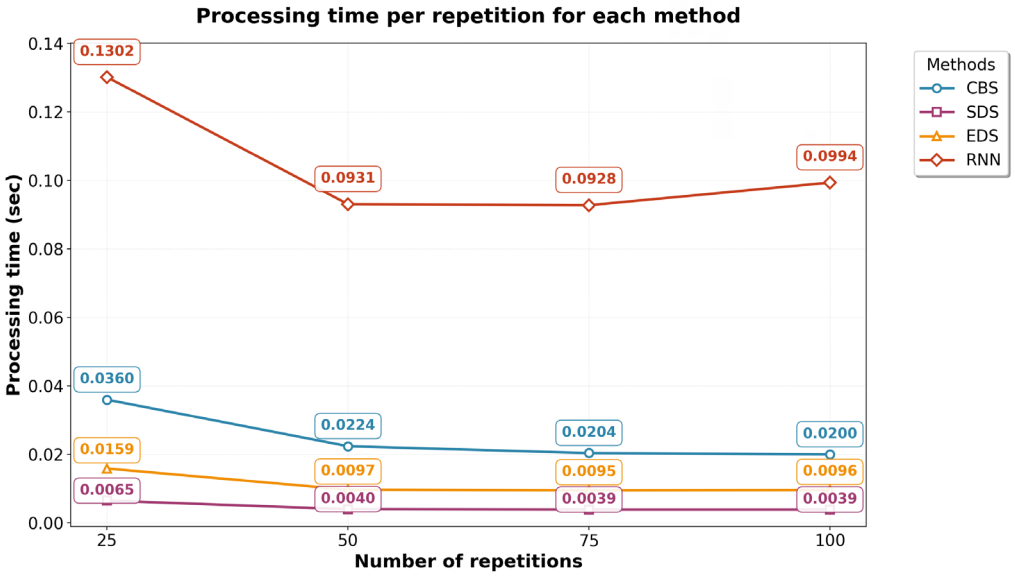

Fig. 13. *Comparison of the computational efficiency of the 4 methods.*
Source: own elaboration.

Thus, in comparison with previous studies, such as[15]-[17], which are based on the use of hyperspectral imagery in the short-wave infrared (SWIR) range, the results obtained in this work show the potential of multispectral data with a low number of bands as a simpler alternative for exploratory detection of materials. This approach therefore represents a relevant contribution compared with previous research aimed at detecting asbestos-cement by means of hyperspectral imagery, since it shows that the use of four- or five-band images makes it possible to significantly reduce both the computational processing costs and the costs associated with data acquisition, compared with those required to capture and process images composed of hundreds of spectral bands. In this sense, the methods that showed greater efficacy and efficiency in this study present a high potential to be articulated in near-real-time monitoring environments for asbestos-cement or other materials of environmental interest, especially in scenarios where access to hyperspectral sensors is limited or unfeasible.

Notwithstanding the above, these findings should be interpreted in light of the geographic and environmental context in which the experiments were carried out. The study is based on data from a single region, with specific surface characteristics and atmospheric conditions, as well as on image properties inherent to the available dataset. Consequently, the results obtained reflect the methodological feasibility of the proposed approach under these particular circumstances, rather than a fully generalizable performance. Any application at a larger scale, whether in operational monitoring contexts or using different types of sensors and environmental configurations, should be considered preliminary in nature and subject to additional validation processes using more diverse datasets and independent reference data.

In this same sense, based on the use in this research of techniques and technologies supported by open-source tools such as rasterio, numpy, pandas, matplotlib and tensorflow, this work becomes a reference to be replicated and extrapolated by universities and research centers, regarding the detection of different materials in multispectral imagery, contributing to addressing the high costs of proprietary tools for processing these images such as ENVI. Likewise, the use of these tools facilitates the simple customization and hybridization of different methods or approaches, which is more complex to achieve in proprietary tools.

Finally, regarding the limitations of this research, it should be mentioned that to enrich the 4-band image, it is first necessary to obtain the additional layer through PCA, which requires additional pre-processing time for the multispectral image, so this must be considered when adapting this approach in real-time monitoring applications. Notwithstanding the above, it was possible to observe that this linking of the 5 bands allows the EDS and CBS methods to obtain more refined results compared with those obtained with the 4-band image.

CONCLUSIONS AND FUTURE WORK

Bearing in mind that although hyperspectral images present computational cost as a challenge due to their high dimensionality, this article proposed as a contribution the implementation and evaluation of methods based on spectral similarity and RNN models for the detection of asbestos-cement in 4- and 5-band multispectral images, in order to determine the effectiveness of each of these methods in detecting this material by using far fewer reflectance bands. The results obtained made it possible to determine that the EDS and CBS methods detected asbestos-cement areas in the multispectral image with good precision. These results allow this research and the methods considered to be extrapolated to the detection of other materials, being an alternative to the acquisition and processing cost of hyperspectral images.

Regarding the limitations of this research, enriching the four-band image by incorporating a component derived from principal component analysis (PCA) requires an additional preprocessing stage, which entails an increase in computational time that must be considered when adapting the approach to real-time processing scenarios. Nevertheless, the inclusion of the fifth band made it possible to improve the stability of the EDS and CBS methods compared with the four-band configuration.

As for the computational efficiency of the evaluated methods, with the 4-band dataset the SDE and EDS spectral distance methods showed no overlap in differentiating the pixel characteristic of asbestos-cement from the sample pixels of other materials, and the EDS method obtained the largest percentage difference between detection thresholds, at 4.364%. In this same sense, although SDE shows no overlap in the thresholds, its percentage difference between thresholds is only 0.067%, which makes it sensitive to classification errors, so that when deployed on the 4-band image it is observed to be the spectral distance method that makes the most classification mistakes. With regard to the results with the 5-band dataset, it is important to mention that the 3 spectral distance methods show no overlap in differentiating the characteristic spectral signature from the non-asbestos sample pixels, and the CBS and EDS methods show the largest percentage differentiation between thresholds, at 2.3% and 3.479% respectively. Thus, the inclusion of an additional band contributes to improving the detection capability of the CBS method, while the differentiation threshold of the SDS and EDS methods decreases slightly. Likewise, as occurs with the 4-band dataset, the SDS method obtains similar results, being the one that makes the most classification errors of the 3 spectral distance methods. On the other hand, with regard to the ANN model, although in the fitting and evaluation it stood out with the training and test set for the datasets derived from the 4- and 5-band images, when the model is deployed on the full image a greater number of classification errors occurs compared with the 3 spectral distance methods, so that vegetation and road pixels are confused with asbestos-cement pixels.

At the computational efficiency level, the 4 methods considered in this research were deployed over a 50x50 pixels region of the image with 5 spectral bands at different repetitions (25, 50,75 and 100). As a result of the evaluation of the methods across the multiple repetitions, the SDS method was found to be the most efficient in processing the image region, with an average time of 4.58 milliseconds, whereas the ANN model was the least efficient, with an average processing time of 103.88 milliseconds. However, at the level of the methods with the best detection effectiveness, the most efficient methods were EDS and CBS, with respective average processing times of 11.18 milliseconds and 24.7 milliseconds, such that the CBS method is 2.22 times slower than the EDS method. These results allow concluding that both the EDS method and the CBS method can be integrated into real-time monitoring systems.

This work made an additional contribution through the use of open-source tools for the pre-processing and detection of asbestos-cement in multispectral imagery by means of spectral similarity methods and ANN models, showing that these libraries and technologies belonging to the Python language were suitable for the experimentation carried out. Thus, the rasterio library was used to obtain the multidimensional array representing the image. Likewise, the numpy and scipy libraries were used for the implementation, evaluation, and deployment of the 3 spectral similarity methods. In the same sense, the tensorflow library was used for the implementation and evaluation of the ANN model architecture. On the other hand, the timeit library was used to run multiple repetitions of the 4 methods considered. Finally, the pandas and matplotlib libraries were used, respectively, to load the points associated with the sample pixels and to display the graphs used in this research. These tools and technologies can be extrapolated to the detection of different materials in multispectral imagery by research centers and universities, taking advantage of the customization and hybridization advantages of these methods in open-source tools.

As future work derived from this research, the first step is to evaluate the effectiveness of machine learning models in the detection of asbestos-cement in 4-band (NIR) multispectral imagery or 5-band imagery, such as those used in this research. Likewise, the aim is to evaluate the detection capability of the spectral similarity methods considered on Sentinel-type satellite imagery with 10 bands, at resolutions of 10 meters.

REFERENCES

[1] C. Zhang, «Introduction to Remote Sensing», en Multi-sensor System Applications in the Everglades Ecosystem, 2020, pp. 31-60. doi: 10.1201/9780429075872-2.

[2] J. Awange, «Fundamentals of Remote Sensing», en Environmental Science and Engineering, 2019, pp. 115-123. doi: 10.1007/978-3-

030-03017-9_7.

[3] W. Fu, J. Ma, P. Chen, y F. Chen, «Remote Sensing Satellites for Digital Earth», en Manual of Digital Earth, H. Guo, M. F. Goodchild, y A. Annoni, Eds., Singapore: Springer Singapore, 2020, pp. 55-123. doi: 10.1007/978-981-32-9915-3_3.

[4] B. Zhang et al., «Remotely sensed big data: evolution in model development for information extraction [point of view]», Proc. IEEE, vol. 107, n.o 12, pp. 2294-2301, dic. 2019, doi: 10.1109/jproc.2019.2948454.

[5] Z. Shun et al., «Research on remote sensing image extraction based on deep learning», PeerJ Computer Science, vol. 8, p. e847, ene. 2022, doi: 10.7717/peerj-cs.847.

[6] A. M. Lechner, G. M. Foody, y D. S. Boyd, «Applications in Remote Sensing to Forest Ecology and Management», One Earth, vol. 2, n.o 5, pp. 405-412, may 2020, doi: 10.1016/j.oneear.2020.05.001.

[7] Z. Wang, Y. Ma, Y. Zhang, y J. Shang, «Review of Remote Sensing Applications in Grassland Monitoring», Remote Sensing, vol. 14, n.o 12, p. 2903, jun. 2022, doi: 10.3390/rs14122903.

[8] M. I. Abdulraheem, W. Zhang, S. Li, A. J. Moshayedi, A. A. Farooque, y J. Hu, «Advancement of Remote Sensing for Soil Measurements and Applications: A Comprehensive Review», Sustainability, vol. 15, n.o 21, p. 15444, oct. 2023, doi: 10.3390/su152115444.

[9] P. Wang, X. Ma, y Q. Zhao, «Learning-based classification approach for coded aperture compressive spectral image», en International Conference on Image, Signal Processing, and Pattern Recognition (ISPP 2023), P. Batista y R. Bilas Pachori, Eds., Changsha, China: SPIE, jun. 2023, p. 137. doi: 10.1117/12.2681198.

[10] A. Bodkin, A. Sheinis, A. Norton, J. Daly, S. Beaven, y J. Weinheimer, «Snapshot hyperspectral imaging: the hyperpixel array camera», en SPIE Proceedings, S. S. Shen y P. E. Lewis, Eds., Orlando, Florida, USA: SPIE, may 2009, p. 73340H. doi: 10.1117/12.818929.

[11] L. Demarchi, A. Kania, W. Ciężkowski, H. Piórkowski, Z. Oświecimska-Piasko, y J. Chormański, «Recursive Feature Elimination and Random Forest Classification of Natura 2000 Grasslands in Lowland River Valleys of Poland Based on Airborne Hyperspectral and LiDAR Data Fusion», Remote Sensing, vol. 12, n.o 11, p. 1842, jun. 2020, doi: 10.3390/rs12111842.

[12] D. Hong et al., «SpectralGPT: Spectral Remote Sensing Foundation Model», IEEE Trans. Pattern Anal. Mach. Intell., vol. 46, n.o 8, pp. 5227-5244, ago. 2024, doi: 10.1109/tpami.2024.3362475.

[13] M. Krówczyńska, E. Raczko, N. Staniszewska, y E. Wilk, «Asbestos—Cement Roofing Identification Using Remote Sensing and Convolutional Neural Networks (CNNs)», Remote Sensing, vol. 12, n.o 3, p. 408, ene. 2020, doi: 10.3390/rs12030408.

[14] F. Frassy et al., «Mapping Asbestos-Cement Roofing with Hyperspectral Remote Sensing over a Large Mountain Region of the Italian Western Alps», Sensors, vol. 14, n.o 9, pp. 15900-15913, ago. 2014, doi: 10.3390/s140915900.

[15] G. Bonifazi, G. Capobianco, y S. Serranti, «Asbestos containing materials detection and classification by the use of hyperspectral imaging», Journal of Hazardous Materials, vol. 344, pp. 981-993, feb. 2018, doi: 10.1016/j.jhazmat.2017.11.056.

[16] G. Bonifazi, G. Capobianco, y S. Serranti, «Hyperspectral Imaging and Hierarchical PLS-DA Applied to Asbestos Recognition in Construction and Demolition Waste», Applied Sciences, vol. 9, n.o 21, p. 4587, oct. 2019, doi: 10.3390/app9214587.

[17] O. Trotta, G. Bonifazi, G. Capobianco, y S. Serranti, «DETECTION OF ASBESTOS CONTAINING MATERIAL IN POST-EARTHQUAKE BUILDING WASTE THROUGH HYPERSPECTRAL IMAGING AND MICRO-X-RAY FLUORESCENCE», Detritus, n.o 21, pp. 27-34, dic. 2022, doi: 10.31025/2611-4135/2022.17233.

[18] M. Hikuwai, N. Patorniti, A. Vieira, G. Frangioudakis Khatib, y R. Stewart, «Artificial Intelligence for the Detection of Asbestos Cement Roofing: An Investigation of Multi-Spectral Satellite Imagery and High-Resolution Aerial Imagery», Sustainability, vol. 15, n.o 5, p. 4276, feb. 2023, doi: 10.3390/su15054276.

[19] D. Enrique Valdelamar Martínez, M. Saba, y L. K. Torres Gil, «Assessment of asbestos-cement roof distribution and prioritized intervention approaches through hyperspectral imaging», Heliyon, vol. 10, n.o 3, p. e25612, feb. 2024, doi: 10.1016/j.heliyon.2024.e25612.

[20] G. E. Chanchí-Golondrino, M. A. Ospina-Alarcón, y M. Saba, «Proposal of a computational method for asbestos detection in hyperspectral images based on the identification of prominent peaks in the spectral signature», rev. investig. desarro. innov, vol. 15, n.o 1, pp. 119-138, mar. 2025, doi: 10.19053/uptc.20278306.v15.n1.2025.19183.

[21] B. G. Ram, P. Oduor, C. Igathinathane, K. Howatt, y X. Sun, «A systematic review of hyperspectral imaging in precision agriculture: Analysis of its current state and future prospects», Computers and Electronics in Agriculture, vol. 222, p. 109037, jul. 2024, doi: 10.1016/j.compag.2024.109037.

[22] N. Ghasemi, J. A. Justo, M. Celesti, L. Despoisse, y J. Nieke, «Onboard Processing of Hyperspectral Imagery: Deep Learning Advancements, Methodologies, Challenges, and Emerging Trends», IEEE J. Sel. Top. Appl. Earth Observations Remote Sensing, vol. 18, pp. 4780-4790, 2025, doi: 10.1109/jstars.2025.3527898.

[23] A. C. Toma, S. Panica, D. Zaharie, y D. Petcu, «Computational challenges in processing large hyperspectral images», en 2012 5th Romania Tier 2 Federation Grid, Cloud & High Performance Computing Science (RQLCG), oct. 2012, pp. 111-114. Accedido: 12 de julio de 2025. [En línea]. Disponible en: https://ieeexplore.ieee.org/document/6528260

[24] S. Li, W. Song, L. Fang, Y. Chen, P. Ghamisi, y J. A. Benediktsson, «Deep Learning for Hyperspectral Image Classification: An Overview», IEEE Trans. Geosci. Remote Sensing, vol. 57, n.o 9, pp. 6690-6709, sep. 2019, doi: 10.1109/tgrs.2019.2907932.

[25] M. E. Paoletti, J. M. Haut, J. Plaza, y A. Plaza, «Deep learning classifiers for hyperspectral imaging: A review», ISPRS Journal of Photogrammetry and Remote Sensing, vol. 158, pp. 279-317, dic. 2019, doi: 10.1016/j.isprsjprs.2019.09.006.

[26] Z. Yu y W. Cui, «LSCA-net: A lightweight spectral convolution attention network for hyperspectral image processing», Computers and Electronics in Agriculture, vol. 215, p. 108382, dic. 2023, doi: 10.1016/j.compag.2023.108382.

[27] U. Ghous, M. S. Sarfraz, M. Ahmad, C. Li, y D. Hong, «EXNet: (2+1)D Extreme Xception Net for Hyperspectral Image Classification», IEEE J. Sel. Top. Appl. Earth Observations Remote Sensing, vol. 17, pp. 5159-5172, 2024, doi: 10.1109/jstars.2024.3362936.

[28] Y.-L. Chang et al., «Consolidated Convolutional Neural Network for Hyperspectral Image Classification», Remote Sensing, vol. 14, n.o 7, p. 1571, mar. 2022, doi: 10.3390/rs14071571.

[29] J. M. Bioucas-Dias et al., «Hyperspectral Unmixing Overview: Geometrical, Statistical, and Sparse Regression-Based Approaches», IEEE J. Sel. Top. Appl. Earth Observations Remote Sensing, vol. 5, n.o 2, pp. 354-379, abr. 2012, doi: 10.1109/jstars.2012.2194696.

[30] X. Huang, P. Wang, S. Zhang, X. Zhao, y Y. Zhang, «Structural health monitoring and material safety with multispectral technique: A review», Journal of Safety Science and Resilience, vol. 3, n.o 1, pp. 48-60, mar. 2022, doi: 10.1016/j.jnlssr.2021.09.004.

[31] L. Wunsch, M. Hubold, R. Nestler, y G. Notni, «Realisation of an Application Specific Multispectral Snapshot-Imaging System Based on Multi-Aperture-Technology and Multispectral Machine Learning Loops», Sensors, vol. 24, n.o 24, p. 7984, dic. 2024, doi: 10.3390/s24247984.

[32] Y. Chen, H. Jiang, C. Li, X. Jia, y P. Ghamisi, «Deep Feature Extraction and Classification of Hyperspectral Images Based on Convolutional Neural Networks», IEEE Trans. Geosci. Remote Sensing, vol. 54, n.o 10, pp. 6232-6251, oct. 2016, doi: 10.1109/TGRS.2016.2584107.

[33] E. Maggiori, Y. Tarabalka, G. Charpiat, y P. Alliez, «Convolutional Neural Networks for Large-Scale Remote-Sensing Image Classification», IEEE Trans. Geosci. Remote Sensing, vol. 55, n.o 2, pp. 645-657, feb. 2017, doi: 10.1109/TGRS.2016.2612821.

[34] F. Melgani y L. Bruzzone, «Classification of hyperspectral remote sensing images with support vector machines», IEEE Trans. Geosci. Remote Sensing, vol. 42, n.o 8, pp. 1778-1790, ago. 2004, doi: 10.1109/TGRS.2004.831865.

[35] R. H. Yuhas, A. F. Goetz, y J. W. Boardman, «Discrimination among semi-arid landscape endmembers using the spectral angle mapper (SAM) algorithm», en JPL, Summaries of the Third Annual JPL Airborne Geoscience Workshop. Volume 1: AVIRIS Workshop, 1992.

[36] N. Audebert, B. Le Saux, y S. Lefèvre, «Beyond RGB: Very high resolution urban remote sensing with multimodal deep networks», ISPRS Journal of Photogrammetry and Remote Sensing, vol. 140, pp. 20-32, jun. 2018, doi: 10.1016/j.isprsjprs.2017.11.011.

[37] F. Martínez-Plumed et al., «CRISP-DM Twenty Years Later: From Data Mining Processes to Data Science Trajectories», IEEE Transactions on Knowledge and Data Engineering, vol. 33, n.o 8, pp. 3048-3061, 2021, doi: https://doi.org/10.1109/TKDE.2019.2962680.

[38] J. Saltz, «CRISP-DM for Data Science: Strengths, Weaknesses and Potential Next Steps», presentado en 2021 IEEE International Conference on Big Data (Big Data), Orlando, FL, USA, 2021. doi: https://doi.org/10.1109/BigData52589.2021.9671634.

[39] C. Schröer, F. Kruse, y J. Gómez, «A Systematic Literature Review on Applying CRISP-DM Process Model.», Procedia Computer Science, vol. 181, pp. 526-534, 2021, doi: https://doi.org/10.1016/j.procs.2021.01.199.

[40] A. M. Shimaoka, R. C. Ferreira, y A. Goldman, «The evolution of CRISP-DM for Data Science: Methods, Processes and Frameworks», Reviews, vol. 4, n.o 1, pp. 28-43, oct. 2024, doi: 10.5753/reviews.2024.3757.

[41] D. Enrique Valdelamar Martínez, M. Saba, y L. K. Torres Gil, «Assessment of asbestos-cement roof distribution and prioritized intervention approaches through hyperspectral imaging», Heliyon, vol. 10, n.o 3, feb. 2024, doi: 10.1016/j.heliyon.2024.e25612.

FUNDING

This article is considered a product derived from the project “Formulation of a comprehensive strategy to reduce the impact on public and environmental health due to the presence of asbestos in the territory of the Department of Bolívar”, funded by the General Royalties System (SGR) of Colombia and identified with the code BPIN 2020000100366. This project was executed by the University of Cartagena, Colombia, and the Fundación Colombia Libre de Asbesto.

CONFLICT OF INTEREST

None

AUTHORSHIP CONTRIBUTIONS

Drafting – original draft: Gabriel Elías Chanchí Golondrino, Manuel Alejandro Ospina Alarcón, Manuel Saba.

Writing–review and editing: Gabriel Elías Chanchí Golondrino, Manuel Alejandro Ospina Alarcón, Manuel Saba.